Diffusion Behavior of Methane in 3D Kerogen Models

Kai Bin Yu[†], Geoffrey M. Bowers[‡], Narasimhan Loganathan[§], Andrey G. Kalinichev[^] and A. Ozgur Yazaydin[*,†]

[†]Department of Chemical Engineering, University College London, London WC1E 7JE, United Kingdom

[‡]Department of Chemistry and Biochemistry, St. Mary's College of Maryland, St. Mary's City, Maryland 20686, USA

[§]Department of Chemistry, Michigan State University, East Lansing, Michigan 48824, USA

[^]Laboratoire SUBATECH (UMR 6457 – Institut Mines-Télécom Atlantique, Université de Nantes, CNRS/IN2P3), Nantes, France

[*]Email: ozgur.yazaydin@ucl.ac.uk

ABSTRACT: As global energy demand increases, natural gas recovery from source rocks is attracting considerable attention since recent development in shale extraction techniques has made the recovery process economically viable. Kerogen is thought to play an important role in gas recovery, however, the interactions between trapped shale gas and kerogen remain poorly understood due to the complex, heterogeneous microporous structure of kerogens. This study examines the diffusive behavior of methane molecules in kerogen matrices of different types (Type I, II, and II) and maturity levels (A to D for Type II kerogens) on a molecular scale. Models of each kerogen type were developed using simulated annealing. We employed grand canonical Monte Carlo (GCMC) simulations to predict the methane loadings of the kerogen models and then used equilibrium molecular dynamics (EMD) simulations to compute the mean square displacement (MSD) of methane molecules within the kerogen matrices at reservoir-relevant conditions, i.e., 365 K and 275 bar. Our results show that methane self-diffusivity exhibits some degree of anisotropy in all kerogen types examined here except for Type I-A kerogen, where diffusion is the fastest and isotropic diffusion is observed. Self-diffusivity appears to correlate positively with pore volume for Type II kerogens, where an increase in diffusivity is observed with increasing maturity. Swelling of the kerogen matrix up to a 3% volume change is also observed upon methane adsorption. The findings contribute to a better understanding of hydrocarbon transport mechanisms in shale and may lead to further development of extraction techniques, fracturing fluids, and recovery predictions.

1. Introduction

Shale gas is attracting considerable attention as an unconventional energy source due to the abundance and geographic distribution of shale as well as the ever-increasing global energy demand.[1,2] Recent advancements in shale gas extraction techniques such as horizontal drilling and hydraulic fracturing, which enhance the extraction volume and shale permeability, respectively, have allowed successful commercial exploitation of shale hydrocarbon resources. However, a recent assessment suggests only up to a fifth of the hydrocarbons in a shale matrix can be recovered using the aforementioned methods.[3] During production, shale gas migrates from the shale matrix to a production wellbore through a network of fractures created by the injection of pressurised fluid;[4–8] typically water, though interest in supercritical carbon dioxide based approaches is growing.[9,10] It has been established that the rate-limiting step in shale gas production lies in the gas migration from the shale matrix of low permeability into the fracture network. Thus, it is of crucial importance to understand the transport of small organic molecules in shale matrices to explain the relatively low yield and rationalize production decline over time.[11–13] Such studies are also needed to identify ways to optimize the shale gas extraction techniques.

Within shale rocks, the majority of the organic material is present as kerogen - a waxy, complex, heterogeneous mixture of hydrocarbons found in organic matter-rich sedimentary rocks deposited in lacustrine, marine, and terrestrial environments around the world. In such an environment, kerogens formed at the end of diagenesis

are slowly buried more deeply in the Earth and undergo thermal maturation (i.e., catagenesis and metagenesis),

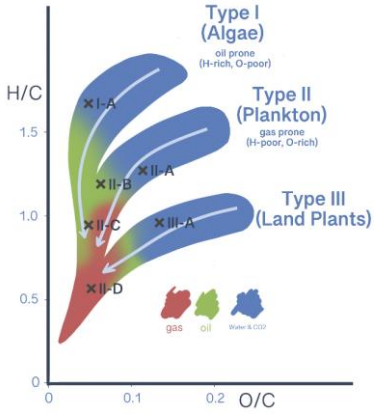

Figure 1: The van Krevelen diagram.[14] The arrows indicate the transformations of kerogens over geological timescale due to thermal maturation, and the crosses mark the kerogen types considered in this work.

during which subsurface thermal stress causes kerogen fragments to break down chemically, eventually (producing oil and gas.[15] Kerogens are insoluble in common organic solvents, such as carbon tetrachloride.[16] Because of their chemical heterogeneity, kerogens are typically classified into three main types based on overall C/H/N ratios determined via elemental analysis. Each type Type I, II, and III) occupies a specific region on the van Krevelen diagram (Figure 1),[14] a plot of H/C ratio against oxygen-to-carbon O/C ratio. The type of kerogen present in a shale depends on numerous factors, including but not limited to its biological origin, depositional environment, burial depth and age/maturity level. Previous research[17–19] reports that the main factor dictating the adsorption capacity of shale samples for CH_4 and CO_2 is their total organic content (TOC), much of which is kerogen. Further studies comparing the adsorption capacity of shale and isolated kerogen samples confirmed the uptake of CH_4 and CO_2 is significantly higher in pure kerogen than that of shale.[20–23] Observing and quantifying the adsorption and transport processes in such systems presents numerous experimental challenges, such as the difficulty in obtaining shale samples and isolating pure, unaltered kerogen as well as the need to examine behaviour over many length and time scales. To mitigate these limitations, classical methods of atomistic computer simulations, such as molecular dynamics (MD) and Monte Carlo (MC) or hybrid MD/MC simulations, provide a convenient way of studying kerogen at a molecular level, providing unique insight into the behaviour of these fluids in nanometer-scale confined spaces. Molecular simulations can provide detailed insight into the kerogen structure and how that structure responds upon fluid uptake/desorption, the rate at which the uptake/desorption occurs, and the effect of fluid–kerogen interactions on adsorption and transport.

However, the complete molecular structure of isolated kerogens is not known, meaning that construction of realistic molecular models remains a challenge. Several experimental techniques, such as solid-state ^{13}C NMR spectroscopy, sulphur X-ray absorption near edge structure (S-XANES), and X-ray photoelectron spectroscopy (XPS), have been used to characterize kerogen samples.[24] These studies identify the elemental composition, the fundamental functional groups and their distribution in the structure, and chemical/structural features present in a given kerogen sample. From these data, realistic two-dimensional (2D) kerogen models can be created with appropriate overall chemical composition and functionality. Thanks to several important studies, detailed 2D molecular diagrams of kerogen have been created for several types and maturity levels. Behar and Vandenbrouke[25] constructed detailed 2D molecular diagrams representative of the three main kerogen types at various stages of their evolution. The model structures they proposed have a high starting molecular weight for the least mature kerogens with decreasing molecular weight as kerogen maturity increases. Their pioneering work enabled Zhang and LeBoeuf[26] to modify the models in their study of the volumetric properties of immature Green River Shale kerogen. In particular, Zhang and LeBoeuf's modification brought the kerogen model in closer alignment with the chemical composition of an extracted immature Green River Shale kerogen. Following a similar approach, Siskin et al.[27] also proposed a 2D Green River oil shale kerogen model consisting of seven unique molecules based on selective chemical derivatizations and NMR spectroscopy. More recently, 3D configurations of kerogen based on Siskin et al.'s model have been built through a combination of *ab initio* and molecular mechanics calculations.[28,29] One common feature of all these models is that the kerogen molecules contain a large number of atoms to duplicate the elemental analysis data. Ungerer et al.[30] overcame this problem by creating six realistic and relatively smaller kerogen models of different types and maturity levels, covering a broad region of the van Krevelen diagram.[14] In addition to constructing models with computational efficiency in mind, incorporating prior knowledge about molecular fragments allowed them to improve kerogen models such that geometrical constraints imposed by (tetrahedral) alkane and (planar) aromatic fragments can be satisfied in 3D. The six kerogen model units are representative of kerogen samples obtained in various depositional environments, where Type I, Type II, and Type III correspond to kerogens of lacustrine, marine, and terrestrial origins, respectively. These individual

molecular units can be used as building blocks to generate larger models of nanoporous kerogen matrices. Since Ungerer et al.,[30] a considerable amount of literature has been published based on their models. More recently, in the same vein, Lee et al.[31] developed three new molecular models for Type II kerogen based on a sample extracted from the Bakken formation.

In a 2016 study, Ho et al.[32] demonstrated that methane release in kerogen matrix is a two-step process, with an initial pressure-driven fast release of free gas followed by a slow release of adsorbed gas through desorption and diffusion across the low permeability kerogen matrix.[33] The second desorption/diffusion step is the rate-limiting step, with diffusion behavior of methane in pores differing from that of bulk methane. Furthermore, Ho and colleagues show that the same packing procedure can give rise to kerogen matrices with different pore connectivity and that some methane might be trapped in isolated pores and non-recoverable. In an investigation into the swelling properties of Type II-D kerogen,[34] they observed swelling of the kerogen matrix following gas adsorption leading to increased surface area, porosity and pore size of the kerogen model. Kazemi et al.[35] calculated both self- and transport diffusion coefficients of methane in a Type II-C kerogen matrix, showing that both converge to a similar value (low diffusivity) as the pressure increases. Michalec and Lísal[36] controlled the microporosity of a Type II-D kerogen model by introducing spherical dummy particles of varying sizes (up to 15 Å) as the kerogen matrices were packed. Subsequently, they compared the adsorption of shale gas on rigid kerogen structures of different microporosity through GCMC as well as MD simulations. The simulated kerogen exhibited lower gas uptake due to lower pore space accessibility, which can be improved by modelling kerogen as a flexible matrix. They also showed that the kerogen matrix preferably adsorbs CO_2 rather than CH_4 due to stronger van der Waals and electrostatic interactions. This result corroborates earlier findings by Sui and Yao[37] and Wang et al.[38] who explored the adsorption of CH_4 and CO_2 in Type II-A kerogen matrix computationally. Through MD simulations, Pathak et al.[39] studied the swelling of flexible Type II-C kerogen

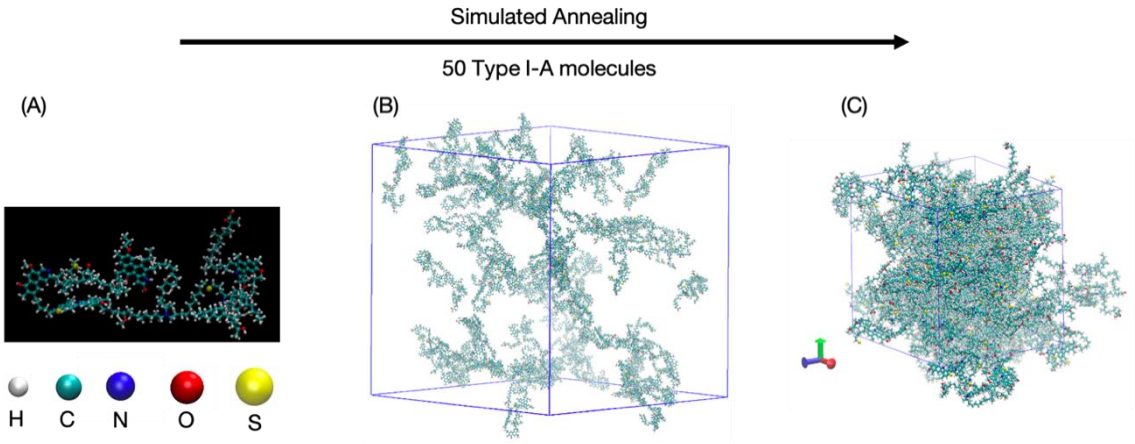

Figure 2: A schematic diagram of the annealing/relaxation procedure. (A) A single Type I-A kerogen unit. (B) The initial configuration of the system before annealing. (C) A kerogen matrix of Type I-A after annealing.

by simulated annealing of kerogen models with a series of 17 fixed mass liquid hydrocarbons. They demonstrated that kerogen exhibits variations in swelling with various organic liquids. Vasileiadis et al.[40] manipulated the porosity of Type II-D kerogen matrices of different system sizes through introduction of dummy particles of different sizes (up to 40 Å) and devised a new algorithm to characterize porosity in kerogen. Their results indicate that system size effects appear to affect the system density and pore size distribution, both of which are also affected by the choice of the force field for the simulations. Pore characteristics, e.g., methane accessible area and volume, increase with increasing number of kerogen units as well as the number of dummy particles and the dummy particle size. In the absence of dummy particles, the pore limiting diameter (PLD) of kerogen matrices is smaller than TraPPE-UA model of CH_4.[41] They suggested using a large system size when simulating kerogen models of this kind. In a separate study, they found that a linear relationship between porosity and adsorption capacity, and that diffusion across kerogen matrices is anisotropic.[42] Zhao et al.[43] and Huang et al.[44] considered the effects of maturity and moisture content and on methane adsorption in Type II kerogen matrices. In both studies, a positive correlation has been shown between methane adsorption and kerogen maturity. This is further supported by a later study by Alafnan et al.[45] Tesson and Firoozabadi[46] reported

methane adsorption in both rigid and flexible Type II-A kerogen and concluded that kerogen flexibility has limited effect on the self-diffusion of methane. It is worth pointing out that while ensuring flexibility of the kerogen matrix, their MD simulations were conducted in the NVT ensemble, where deformation was not accounted for. Wu and Firoozabadi[47] conducted boundary-driven non-equilibrium molecular dynamics (BD-NEMD) simulations to study the transport of methane across a matrix comprises of 60 Type II-A kerogen molecules. They noted that a reduction in the CH_4 flux is primarily driven by the change in pore size and shape as the kerogen matrix was flexible. He et al.[48] developed a new model to quantify the diffusive tortuosity of kerogens based on Type II-C kerogen. In order to realistically model mature Type II kerogens, Rezlerová et al.[49] modelled embedding of various molecules in the kerogen matrices of Type II-C and Type II-D through annealing dynamics, thereby inducing microporosity. They also subsequently introduced mesoporosity by creating a slit-shaped mesopore of varying sizes (i.e., 20 or 30 Å) between the replicated matrices to model a multi-scale pore network. They computed the adsorption isotherms of pure CH_4 and a binary equimolar mixture of CH_4 and CO_2 for their models and also evaluated the self-diffusivity of CH_4 and CO_2. They noted that an overmature Type II-D kerogen has a higher accessible surface area than a mature Type II-C kerogen due to the preferential parallel stacking of the overmature kerogen macromolecules. In addition, this stacking arrangement in the overmature kerogen creates a less tortuous micropore network, such that the self-diffusivity of CH_4 is higher than that in the mature kerogen. Their study also complements the conclusions from other studies[36–38] that kerogens are relatively selective towards CO_2 vs. CH_4. Comparably, Sun et al.[50] represented fractures in kerogen using slit-shaped nanopores of different sizes (up to 15 Å) and studied adsorption and diffusion of pure gas and a binary mixture of CH_4 and CO_2 in Type II-D kerogen. They found that the kerogen matrix preferably adsorbs CO_2 more than the slit mesopores. Both studies observed that the CH_4 adsorption isotherm in kerogen follows type-I Langmuir adsorption behavior. Li et al.[51] conducted MD simulations to study CO_2 storage in water-filled slit-shaped nanopores of different sizes through a kerogen matrix of the Type II series. Chong et al.[52] cluster size analysis showed the existence of pore discontinuity upon adsorption of CH_4 and CO_2, whereas with water, continuity can be observed in the micropores of Type II-A kerogen matrix. In addition, results from multiple investigations[37,43,52–54] into immature Type II-A kerogens with different starting number of kerogen macromolecules have demonstrated that despite achieving similar final simulated density, the differences in the porosity of the resulting packed molecular structures can be as high as an order of magnitude. More recently, Li et al.[55] attempted to shed some light on Schroeder's Paradox,[56] which suggests a discrepancy in solute sorption exists when a polymer is exposed to solvent in saturated vapor and pure liquid states, concerning kerogen systems. By employing hybrid MD-GCMC simulations, they reported that liquid-induced kerogen swelling is greater than that of their gas counterparts.

Together, these studies highlight the complexity of kerogens and that they assume a broad spectrum of pore characteristics (connectivity, constrictivity and tortuosity).[57,58] Adding to the complexity, the use of different kerogen model molecules and packing/annealing procedures may lead to different results. Whilst all the models described here are chemically representative, it is unclear how structurally descriptive they are compared to pure isolated kerogen or kerogen as it would be found in a field sample of shale. Generating a reliable and controlled distribution of 3D kerogen structures remains challenging, particularly given the limited experimental data to use as blueprints for guidance. Given these challenges, in this study we set out to qualitatively assess the diffusion behavior of methane in kerogen matrices constructed from model kerogen molecules representing different types and maturity at conditions relevant to a geological shale-gas reservoir (365 K and 275 bar). A sufficiently large number of macromolecules (i.e., 50) were used to avoid system size effects noted in the literature and no dummy particles were involved to introduce porosity. Unlike earlier studies, in order to mimic reservoir conditions and allow realistic deformation (swelling) of the kerogen matrices, here we computed the MSD of CH_4 in hundred nanosecond long MD simulations via both NVT and NPT statistical ensembles. To the best of our knowledge, this is the first study to include all major kerogen types, enabling this work to provide a broader overview of CH_4 diffusion in kerogens.

2. Methods

Whilst the exact structures of bulk kerogen are unknown, many researchers have utilized simulated annealing procedures to construct model kerogen matrices out of several model kerogen molecules (Figure 2), where a number of molecular units of a kerogen type are first placed in a large simulation box (low initial kerogen density). The box is subsequently equilibrated through a series of cooling and heating cycles, often in a stepwise manner and at high pressure, resulting in a condensed structure, i.e., a matrix. The density of the final

configuration is then compared against experimental data of the corresponding kerogen type to validate the packed structure.

Creation of Bulk Kerogen Matrices

The relaxation procedure set out by Michalec and Lísal[36] was closely followed to prepare the initial configuration of bulk kerogen matrices. 50 kerogen macromolecules were randomly inserted into a large cubic simulation box with an initial system density of ~0.05 g/cm^3 to avoid interactions with copies of their images through the imposed periodic boundary conditions. This was done for each kerogen type reported by Ungerer et al.[30] Then the systems were relaxed through energy minimization via steepest descent, followed by annealing dynamics. A total of 12 cycles were executed as described in Table 1. The choice of final temperature and pressure represents a typical shale reservoir at ~3-4 km depth. Figure 3 shows the changes in system density during annealing for Type I-A system, as an example. To

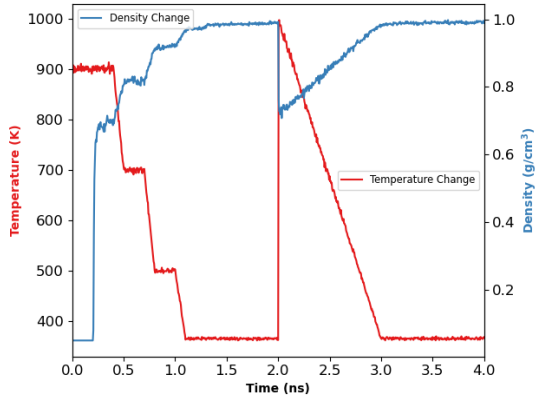

Figure 3: Heating and cooling profile during annealing dynamics for Type I-A kerogen.

reduce the statistical uncertainty, this relaxation procedure was carried out with ten independent runs, and to check for convergence, the final system density of 10 matrices was then averaged and compared to experimental data. We then randomly selected three of the 10 relaxed matrix structures for the subsequent grand canonical Monte Carlo simulations (GCMC).

GCMC

GCMC simulations were employed to compute CH_4 loading in selected matrices for each kerogen type. In the grand canonical ensemble, the chemical potential (μ), volume (V) and temperature (T) of the systems are fixed whereas the number of molecules fluctuate. The GCMC simulations allowed us to compare variations in CH_4 loading due to packing as well as to determine the number of CH_4 molecules to insert in the kerogen matrices for MD simulations.

Molecular Dynamics

In order to generate the initial configurations for MD simulations, one of the three kerogen matrices used in the GCMC simulations was selected for each type of kerogen. We randomly inserted the number of CH_4 molecules corresponding to the predicted CH_4 loadings from GCMC simulations into the kerogen matrices. The steepest descent algorithm was used to relax the CH_4 loaded systems to avoid bad contacts. Then, the systems were subjected to an NVT MD run and successively an NPT run, both for 100 ns where N, V, T and P represent the number of atoms, volume, temperature, and pressure, respectively. In order to minimize statistical error, we performed five independent MD simulations for each kerogen type, with randomly determined different initial CH_4 positions in the matrix. Finally, we computed the mean square displacement (MSD) of methane molecules for each kerogen matrix in all three directions of Cartesian space. The entire workflow for simulations is illustrated in Figure S1.

Table 1: The annealing procedure for the creation of kerogen matrices.

Ensemble	*T* (K)	P (bar)	*t* (ns)
NVT	900	–	0.2
NPT	900	10	0.2
NPT	900 → 700	10	0.1
NPT	700	10	0.2
NPT	700 → 500	10	0.1
NPT	500	10	0.2
NPT	500 → 365	10	0.1
NPT	365	10	0.2
NPT	365	10 → 275	0.2
NPT	365	275	0.5
NPT	1000 → 365	275	1.0
NPT	365	275	1.0

Kerogen and Methane Interaction Potentials

A number of force fields have been used to model kerogen, including but not limited to, COMPASS,[59] CVFF,[60] DREIDING,[61] GAFF,[62] and PCFF+.[30] PCFF+ was originally used in the development of kerogen model units by Ungerer et al.[30] However, the short-range non bonded interactions in PCFF+ are described by a repulsive–attractive 9-6 Lennard-Jones (LJ) potential, which is incompatible with many other force fields that include a 12-6 LJ potential, such that it is difficult to simulate kerogen with other compounds. CVFF is one of the most commonly used force fields in kerogen simulations,[32–34,36,51,52] and the 12-6 LJ potential in its

functional form is compatible with other force fields. CVFF correctly reproduces the experimental density of the Type II kerogen series[51] and provides a reasonable description of kerogen interactions with its constituents, e.g., carbon dioxide (EPM2),[63] methane (TraPPE-UA),[41] and water (SPC).[64] The partial atomic charges of CVFF atoms were assigned using a bond increment scheme. In this study, we further extended the application of CVFF to model two additional immature kerogen types, namely, Type I-A and Type III-A. Methane molecules were represented by the TraPPE-UA model,[41] which has been shown to correctly predict thermodynamic properties and reproduce experimental phase equilibrium data. The relevant simulation input files and force field parameters used in this work can be found in the supporting information section.

Simulation Settings

RASPA molecular simulation package[65] (2.0.39) was used for GCMC simulations. Each GCMC run included a 5×10^5 initialization cycle followed by a 5×10^5 production cycle, where each cycle is N steps. N is equal to the number of particles present in the system. Owing to the enormous number of atoms involved, for computational efficiency, kerogen structures at this stage were treated as a rigid framework, and the methane-kerogen interactions were pretabulated. During the GCMC simulations, insertion/deletion, translation and reinsertion of methane molecules were sampled with equal probability (approx. 33 %). The acceptance rules for insertion and deletion in the grand canonical ensemble included fugacity, a measure of chemical potential, and was calculated using the Peng–Robinson equation of state for methane.[66]

All MD simulations were performed using GROMACS 2020.4 molecular dynamics simulation software.[67] A time step of 0.5 fs was used in the integration of Newton's equations of motion via the leapfrog algorithm. During the annealing procedure, a velocity rescaling thermostat[68] was used to control the system temperature, whereas during the MD production runs, a Nosé–Hoover thermostat[69,70] with a coupling time of 0.1 ps was used. In the NPT simulations, the pressure was maintained using an anisotropic Parrinello–Rahman barostat[71] with a coupling time of 0.5 ps, such that all three dimensions of the systems were allowed to fluctuate independently to allow realistic deformation of kerogen matrices. Long range Coulombic interactions were calculated using a smooth particle mesh Ewald (PME) method[72] of a fourth order polynomial with a mesh width of 0.12 nm.

In both MD and MC simulations, periodic boundary conditions were applied in all three directions. LJ potential was used to describe short-range non-bonded interactions. The LJ interactions of unlike atom pairs in different molecules or further than 3 bonds of the same molecule were calculated using the Lorentz-Berthelot mixing rules. A cut-off radius of 14 Å was used for the LJ interactions and the real part of the Ewald summation. Long-range dispersion corrections were not applied to energy or pressure. All simulations were carried out at 365 K and 275 bar unless stated otherwise. Sample input files, including force field parameters, from MD and GCMC simulations are provided in the Supporting Information.

Utilising PoreBlazer v4.0,[73] a grid-based algorithm was used to calculate and characterize the porosity of the kerogen matrices, before and after the MD simulations. Settings in PoreBlazer were modified such that CVFF interaction parameters, 14 Å cut-off radius, and the cubelet size of 0.2 Å were used in the calculations. Pore limiting diameter, which is defined as the maximum penetrant diameter where a pore network remains percolated, was calculated. In addition, accessible pore volume was estimated with the Widom's ghost atom insertion method[74] by using a helium probe, with parameters taken from Hirschfelder et al.,[75] where $\sigma_{He} =$ 2.64 Å and $\varepsilon/k_{B_{He}} =$ 10.9 K. Accessible geometric surface area of the kerogen matrices was calculated using a N_2 probe of size 3.314 Å.[76]

3. Results and Discussion

Kerogen Model Validation and Characterization

Before investigating the effects of anisotropy and heterogeneity of the different kerogen matrices, we validated the CVFF force field to ensure the calculated densities of the kerogen matrices are comparable to experimental data. For each kerogen type, we created 10 condensed kerogen matrices, each starting from a random initial configuration of kerogen molecules, using the simulated annealing procedure outlined in the methods. Table 2 shows the average simulated density of six kerogen types in comparison to relevant experimental data. The density of Type I-A compares quite well with the Green River Shale sample. However, the densities of the Type II kerogen series appear to be slightly lower or close to the lower bound of experimentally measured Kimmeridge Clay kerogen densities, except for Type II-B for which we found no experimental comparison set in the literature. A possible explanation for this might be that Ungerer et al.'s Type II kerogen model molecules[30] are based on Duvernay kerogen samples. It is well understood that kerogens of the same maturity may exhibit different chemical compositions,[24] even when extracted from the same geological site. In addition, their

composition is also dependent on the evolutionary history of the sedimentary formation that they formed in and the heterogeneity in composition of kerogen samples. Experimental data[77] suggest that Duvernay kerogens have a density range of 1.28 ± 0.3 g/cm^3, which our results fit well. Similarly, the same explanation applies to Type III-A kerogen,[24] since the calculated density is reasonably close to the lower boundary of the reported range. A comparison of our results with the density of Type II

Table 2: Comparison of experimental and averaged simulated kerogen densities at 365 K and 275 bar.

Kerogen Type	Source	Density (g/cm^3)	
		Experimental	Simulated
I-A	Green River Shale	0.95[78]	0.964 ± 0.004
II-A	Kimmeridge Clay Formation	1.18–1.29[79]	1.117 ± 0.008
II-B	-	-	1.080 ± 0.017
II-C	Kimmeridge Clay Formation	1.18–1.25[79]	1.138 ± 0.022
II-D	Kimmeridge Clay Formation	1.30–1.40[79]	1.305 ± 0.015
III-A	Blanzy–Montçeau Basin	1.16-1.20[80]	1.119 ± 0.060

kerogens from other modelling studies shows that our results are slightly lower than the reported values. It is important to highlight that during the initial step of our packing procedure, the kerogen units were inserted randomly to account for a wide range of structural variations, whereas most researchers[36,46,52] considered limited cases, where the kerogen macromolecules were oriented in the same direction, with the assumption that they will ultimately evolve into a uniformly layered kerogen matrix. Furthermore, the discrepancy between our results and those of other Type II modelling studies could be attributed to the packing procedure and conditions or the number of kerogen molecules involved. Vasileiadis et al.[40] reported system size effect when using kerogen models of the same kind, where system density decreases as the number of kerogen molecules increases. It seems possible that these results are related to the favorable stacking of the polyaromatic units of kerogen macromolecules,[81] where pores in one direction may be elongated and cause reduction in system density. Overall, the simulated density of kerogen matrices is in the range of 0.96 – 1.20 g/cm^3 which is in line with the general trend of the available experimental and modelling data.

GCMC Simulations

To account for structural variation that arises during the annealing procedure caused by the random initial configurations of the kerogen units used, we first randomly chose three of the 10 packed structures for each kerogen type for a consistency check. First, we perform GCMC simulations to determine their CH_4 adsorption capacity. Table 3 shows an overview of methane adsorption for the kerogen matrices estimated via GCMC simulations. It is apparent that immature kerogen of Type I has the lowest methane uptake, followed by relatively moderate and high methane adsorption capacity for Type II-A and Type III-A immature kerogens, respectively. In addition, the CH_4 adsorption capacity increases with thermal maturity in Type II kerogen series. These results match those observed in earlier modelling studies[43–45,49,53] and experimental measurements.[82–86] The CH_4 adsorption capacity was found to be highest in Type II-D kerogen compared to the other kerogen types.

The amount of CH_4 loading has a positive correlation with increasing aromatic content of the kerogen units, where Type II-D kerogen has the highest percentage of aromatic content of all.[30] This can be explained by the preferential parallel stacking of the polyaromatic parts of the kerogen macromolecules,[81] and hence larger accessible surface area, resulting in increased CH_4-kerogen interactions.[49] The results of the aforementioned relationships are depicted in a 3D scatter plot in Figure 5.

Table 3: The amount of CH_4 loading in various rigid microporous kerogen matrices obtained via GCMC simulations at 365 K and 275 bar.

Kerogen Type	Loading (mmol/g)
I-A	0.430 ± 0.002
II-A	0.683 ± 0.001
II-B	1.353 ± 0.001
II-C	1.363 ± 0.002
II-D	2.034 ± 0.004
III-A	1.969 ± 0.002

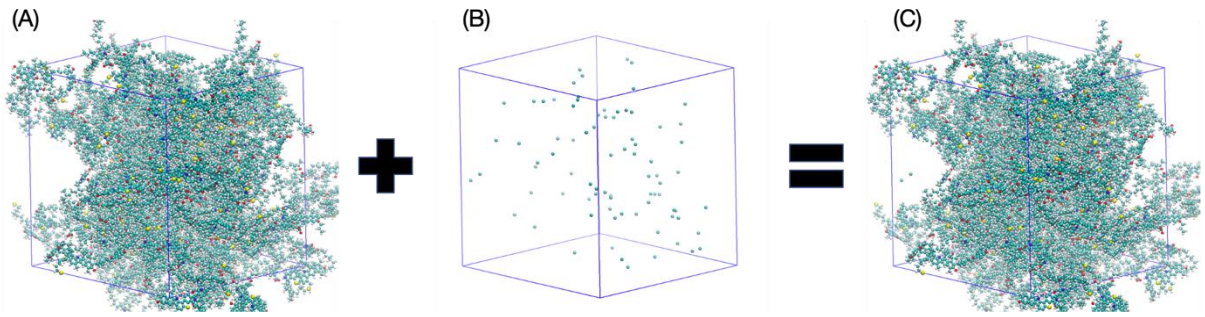

Figure 4: A schematic diagram of the preparation of kerogen matrix loaded with methane. (A) An unfilled kerogen matrix. (B) A random initial configuration of methane molecules, where the capacity was pre-determined through GCMC. (C) A filled kerogen matrix.

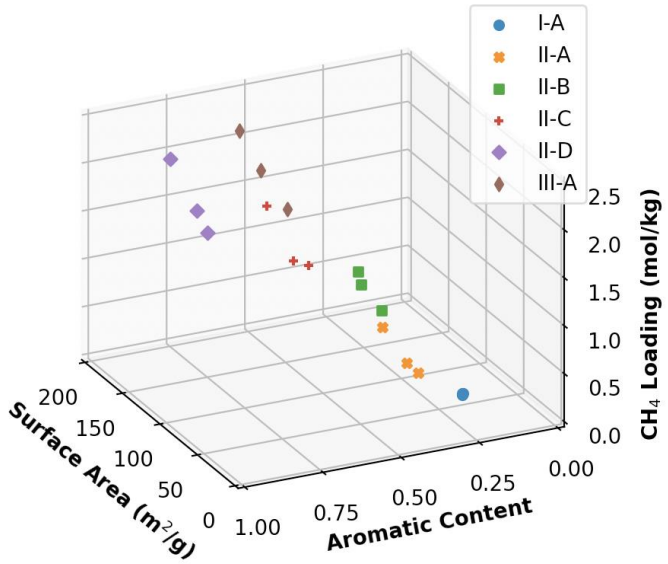

Figure 5: The amount of CH_4 loading versus the surface area of 3D kerogen models of various types and the fraction of its aromatic carbon content.

From the chart, there is a clear trend of increasing CH_4 loading with the increase of the aromatic carbon content and surface area of the kerogen matrices. Closer inspection of the figure shows that the surface areas of the considered kerogen matrices are not uniform, and this is likely due to the packing procedure that we employed. The computed methane uptake in our overmature Type II-D kerogen models, which did not have any artificially induced microporosity, is 2.5 times higher than thatreported by Michalec and Lísal.[36] A possible explanation for this might be that Michalec and Lísal[36] used a smaller number of kerogen molecules and are therefore more susceptible to finite size effects. It has been reported that structural properties such as methane accessible area changes with the number of macromolecules as well as the packing procedure used.[37,40,43,52–54] As a result, the pore network characteristics of the packed structures from our studies are likely to differ from other studies whether artificial porosity is introduced in those studies or not. As a result of these size effects and a limited sample size, the relationship between pi stacking and increased surface area might not generalize for other kerogen types or packing methodologies.

Methane Self-Diffusivity

Diffusion is the primary mode of gas transport in shale rocks, making diffusion rates crucial for understanding hydrocarbon recovery and the factors that influence it. Anisotropic behavior of shale rocks as a result of shale bedding has been found to influence permeability. A number of recent studies[38,42] have reported anisotropy in Type-II kerogen structures. To improve our understanding of shale gas transport mechanisms (i.e.,

mainly CH_4), we computed the MSD of pure CH_4 along all three Cartesian directions in kerogen matrices of different types and maturity levels. Isolated and connected pores exist in kerogen and will almost certainly affect methane uptake and mobility; thus, we randomly inserted CH_4 into the selected kerogen matrices to evaluate the effect or pore network accessibility on CH_4 self-diffusivity. For each kerogen type, five CH_4-

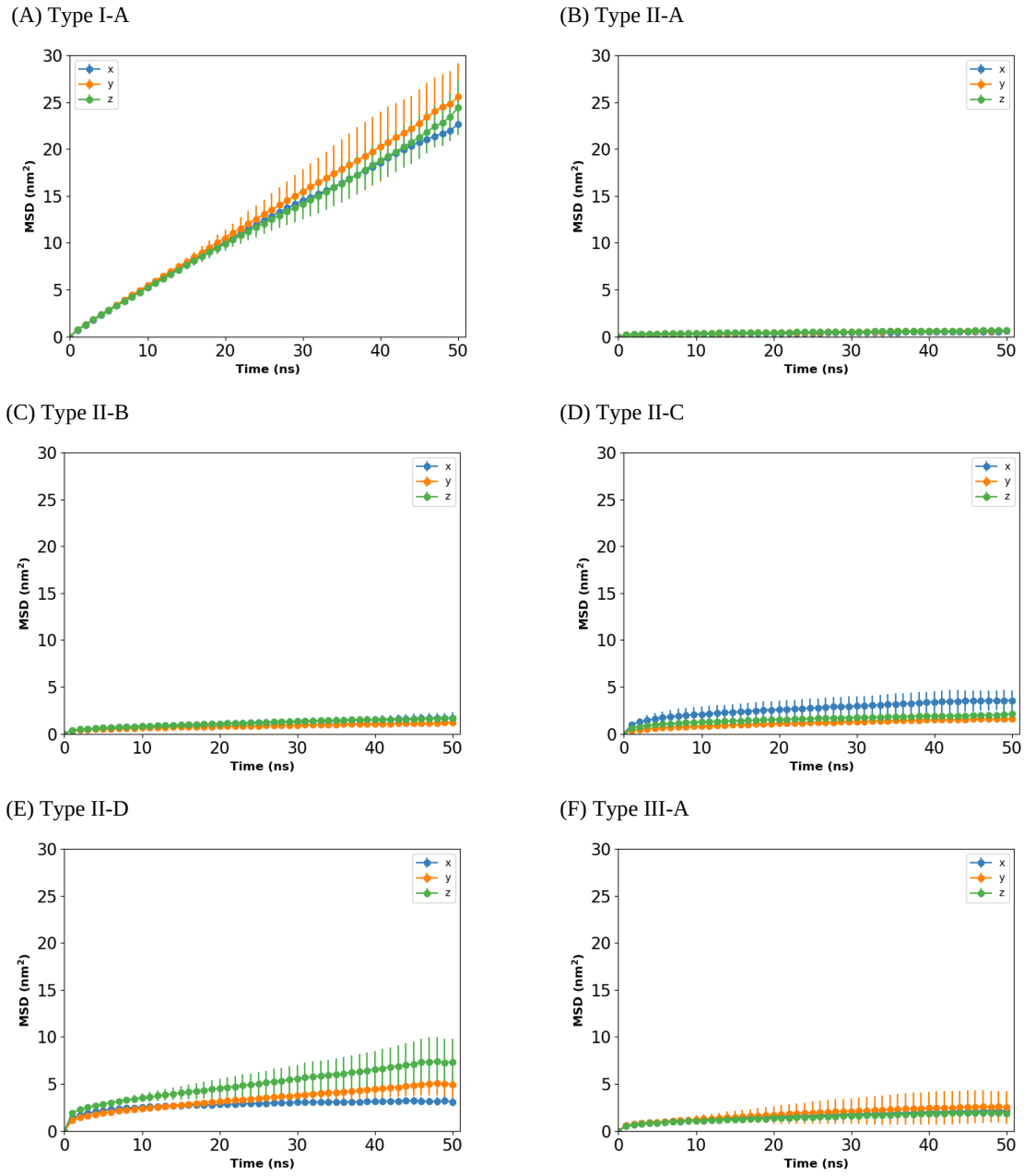

Figure 6: The averaged MSD plots of CH_4 in the x, y and z directions from five independent NPT ensemble MD simulations in six kerogen types at 365 K and 275 bar. Refer to Figure S3 for unscaled version of each plot and Figure S6 for analysis of anisotropy in MSD of methane molecules.

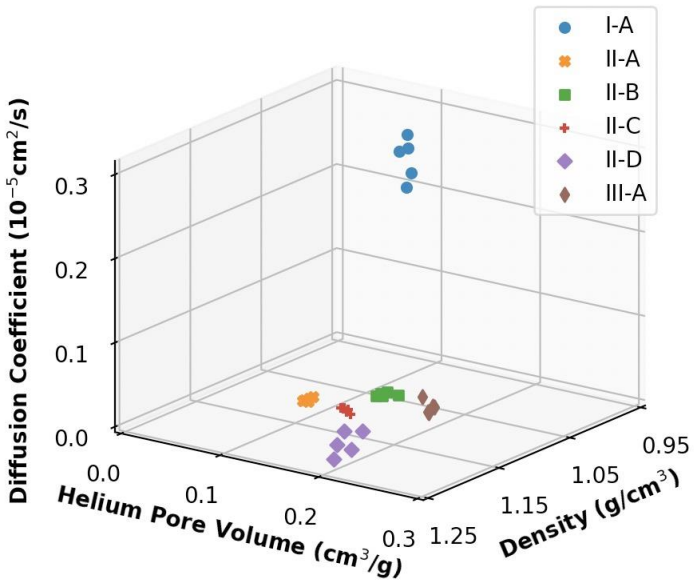

Figure 7: Diffusion coefficients of CH_4 in kerogen matrices of various types versus its density and helium accessible pore volume.

loaded matrix configurations were generated such that each configuration had different initial positions of CH_4. A total of 30 EMD simulations were performed, i.e., five for each kerogen type. Figure 6 displays the averaged MSD plots for CH_4 in various kerogen matrices over the last 50 ns in the NPT ensemble at 365 K and 275 bar. Similar to the earlier observation, Type I-A kerogens exhibit isotropic behavior with no appreciable difference in the MSD in any direction (Figure S6). Looking at the MSD plots for Type II-A and Type II-B kerogens, there appears to be 2D planar regions where the diffusion rate is similar and differs from that perpendicular to the plane. MSD plots of Type II-C show a large standard deviation for the x-component but a low standard deviation for their y-component, suggesting a more uniform interconnected pore structure such as a channel in the y-direction. Both MSD plots for the Type II-D and Type III-A kerogen models show a similar behavior to that of Type II-C kerogen. Furthermore, radial distribution function plots methane with atoms of different functional groups present in kerogen models show that predominant methane binding sites may vary from one kerogen model to another. Due to the specific composition of the model and the specific conformations limiting access to certain types of sites for some models. But overall, it appears that sulfur, nitrogen and oxygen atoms of different functional groups provide the majority of preferred binding sites.

Figure 7 presents the 3D scatter plot of the relationship between the diffusion coefficients of CH_4 and the density and pore volume of the swollen kerogen matrices. The most interesting aspect of this graph is that, apart from Type I-A kerogens, a positive correlation is found between the diffusion coefficients of CH_4 and the pore volume of kerogens. The most unexpected result is the anomalous CH_4 diffusion rate in Type I-A kerogens, which suggests that there are other factors at play that affect the CH_4 diffusion in kerogen matrices. The observed increase in CH_4 diffusion could be attributed to the lack of aromatic carbon in Type I-A kerogens, where less stacking could potentially create more diffusion paths, such that CH_4 could permeate easily in all three directions, i.e., isotropic diffusion. The percentage of aromatic groups in kerogen molecules increases from Type I to Type III kerogen, with the highest in Type II-D kerogen. The increase in polyaromatic regions of the kerogen units and subsequent stacking of these regions may result in a matrix that is not amorphous and hence create a system with anisotropy. The MSD of CH_4 in Type I-A kerogen is an order of magnitude higher than the other kerogen types, which suggests that in Type I-A, CH_4 has the fastest diffusion rate compared to other kerogen types. This makes sense in light of the lower density of this material and the larger size of the molecular units, leading to a packed structure with greater pore volume and connectivity compared to the other packed models. The lowest diffusion rate is observed for the Type II-A kerogen. The results from the Type II kerogen series further support previous findings[38,42] that diffusion behavior of CH_4 in Type II kerogens is anisotropic, although many of the observed differences occur within the error bars on each plot. The magnitude of the standard deviations can be attributed to different pore space accessibility as a result of several factors outlined above. In general, the magnitude of the standard

deviations is similar between different plots (typically fractions of a nm^2 at early stages of the simulations and roughly 2-4 nm^2 - after 50 ns) and is on the same order of magnitude for each direction.

Volume Changes up on CH_4 Adsorption

Table 4 compares the structural properties of the kerogen matrices before and after MD simulations, showing that kerogens experience volumetric strain upon CH_4 adsorption. This is consistent with other literature data.[34,37] In addition, the pore limiting diameter of all kerogen matrices appears to be smaller than the methane molecular diameter in the TraPPE-UA force field, i.e., 3.73 Å. This suggests methane should not be able to diffuse through the percolated pore network. Yet some diffusion is observed, most notably in the Type I-A model (Figure 5). This finding is consistent with the trend reported in an earlier study[40] for Type II-D kerogen. Diffusion of CH_4 through pores that are too small to permit methane motion suggests that the CH_4 molecules themselves may actively change pore accessibility, opening up micropores that were previously inaccessible. Indeed, pore size distribution analyses of kerogen models before and after the MD simulations suggest that methane imbibition has caused a shift of pore size distribution from the initial peak at approx. 3.2 Å to 3.8 Å, which is about the size of a TraPPE united atom methane molecule (Figure S4). Slow diffusion observed in kerogen types other than Type I-A could be due to CH_4 molecules being confined and localized in small nanospaces, i.e., isolated pores with no diffusion pathways. Finally, total helium volume of the kerogen matrices appears to have increased after CH_4 adsorption, which suggest that CH_4 adsorption increases the porosity of the matrices, consistent with the hypothesis that CH_4 actively opens diffusion pathways. Additional studies that can provide energetic insight into this process are warranted. Vasileiadis et al.[42] reported that the self-diffusion coefficient has a positive correlation with the pore limiting diameter. However, the findings of this study do not support their results. However, the findings of this study do not support their results. In any case, construction of 3D kerogen matrices from relatively low molecular weight kerogen macromolecules should be handled with care as the lack of cross-linking between kerogen units may allow increased flexibility which is not present in real kerogen.[36]

Table 4: Properties of six kerogen models before and after five MD simulation runs.

Property	Kerogen Type	Initial	Final*	Change (%)
Volume (nm^3)	I-A	328.58	330.06 ± 0.97	0.45
	II-A	289.11	290.30 ± 0.91	0.41
	II-B	262.33	265.13 ± 1.25	1.07
	II-C	250.45	253.56 ± 0.54	1.24
	II-D	161.04	165.25 ± 0.77	2.62
	III-A	249.08	252.08 ± 0.74	1.20
Pore limiting diameter (Å)	I-A	1.580	1.578 ± 0.183	-0.13
	II-A	1.540	1.542 ± 0.098	0.13
	II-B	1.890	1.892 ± 0.190	0.11
	II-C	2.460	2.460 ± 0.284	0.00
	II-D	2.930	2.932 ± 0.544	0.07
	III-A	2.960	2.956 ± 0.445	-0.14
Helium accessible pore volume (cm^3/g)	I-A	0.061	0.074 ± 0.002	21.64
	II-A	0.071	0.085 ± 0.002	19.72
	II-B	0.117	0.137 ± 0.004	17.44
	II-C	0.118	0.142 ± 0.002	20.00
	II-D	0.176	0.216 ± 0.006	22.84
	III-A	0.167	0.193 ± 0.004	15.57

* Average volume of the final frames of 5 independent MD runs.

4. Conclusions

The primary motivation of this study was to examine CH_4 diffusion in 3D kerogen matrices built from model kerogen molecules that span the recognized types and maturity levels of natural kerogens. The MD and GCMC simulation results reported here show that swelling of the 3D kerogen matrix occurs upon CH_4 adsorption. Methane adsorption also induces other changes in the pore network such as variations in the pore limiting diameter and accessibility between pores in the network. Importantly, all kerogen structures exhibit some degree of anisotropy in the CH_4 diffusion behavior with the exception of Type I-A kerogen (Figure S6), the least mature and lowest density model. As has been observed for fluid diffusion in other microporous to nanoporous materials, the diffusion of CH_4 in kerogen matrices is slow compared to bulk CH_4.

This study has many broader implications for understanding CH_4 diffusion and recovery in kerogens and shales. The scientific community already knows that kerogens contain a significant fraction of the methane in shale-gas reservoirs[87–89] and that the recovery of methane from shale-gas reservoirs is low compared to other types of gas reservoirs (a few 10s of %).[90,91] What is less clear is why the recovery is so low and what can be done about it. The solutions to both of these questions rely on a detailed molecular-scale understanding of methane behavior in shales and all shale components, including kerogen. The ability to extract kerogen and know the extracted kerogen has the same physical and chemical characteristics as kerogen in the native rocks is currently limited. Thus, computational approaches are likely key to developing a molecular-scale understanding of what is happening in shale-gas reservoirs, and will also be needed to help verify experimental data once the community at large is able to collect detailed molecular-scale experimental data for methane adsorption and dynamics in kerogens. Thus, there is a pressing need to have good computational models of kerogens, to understand how to build realistic computational models of kerogens, and to do both of these for a broad range of kerogen types. Due to the scope of the kerogen models examined in this study and the clear procedures for generating kerogen matrices, one of the more important broader implications of the present study is that it forms an important baseline data set for future research into gas recovery from kerogen. These results also highlight several operational considerations that must go into creating computational models of kerogen and interpreting and comparing the associated molecular modelling data sets. Operationally, the annealing procedure employed when creating a 3D kerogen matrix from small representative model molecules plays an important role in determining the final pore characteristics of the dense kerogen structures. More research is needed to understand the relationship between the annealing method and the pore accessibility of the resulting packed structures. To improve consistency between modelling studies and applicability to the field, our results and those in the literature also suggest that more experimental data are required regarding the pore network and network connectivity and that future modelling studies must map the model kerogen matrix pore network to match these data. Based on the volume expansion and potential active role of CH_4 in the pore network, future work should be conducted under NPT conditions to enable swelling of the kerogen matrix. Likewise, additional modelling studies that estimate the energetics of methane adsorption and kerogen matrix swelling are warranted to improve our understanding of CH_4 transport thermodynamics in this important phase of shale gas reservoirs. The results presented here make it possible to conduct new and much needed modeling calculations of thermodynamic parameters regarding methane adsorption in a broad array of kerogen types, transport calculations, and computational models of methane/water and methane/carbon dioxide competition for binding sites in kerogens. The results presented here show that mature kerogens have more anisotropic diffusion pathways than immature kerogens and that it should be easier to recover methane from kerogen types with higher methane diffusivities and when the kerogens have the physical space required to swell since the flexibility of the kerogen network seems key to enabling methane diffusion. The latter point is particularly important given the known volume expansion of shales due to water uptake by clay minerals, which may alter the pore network and kerogen density/porosity.[4] Ultimately, a detailed molecular-scale understanding of methane-kerogen interactions from this and future studies using similar methods of constructing kerogen models will contribute to practical in-field solutions for increasing the methane recovery from kerogens in shales.

5. Supporting Information

A workflow diagram of the simulation set up procedure. The average MSD of CH_4 in the x, y and z directions in six kerogen types in NVT and NPT ensembles. Normalised MSD of CH_4 in kerogens. Pore size distributions of kerogens before and after methane loading. RDFs between CH_4 and between atoms of different functional groups in kerogen macromolecules of various types. Files containing simulation input parameters.

Acknowledgements

We dedicate this paper to our beloved colleague R. James Kirkpatrick whom we lost not long ago. The authors acknowledge the use of the UCL Myriad High Performance Computing Facility (Myriad@UCL), and associated support services, in the completion of this work. We are grateful to the UK Materials and Molecular Modelling Hub for computational resources, which is partially funded by EPSRC (EP/P020194/1 and EP/T022213/1). The authors acknowledge financial support from the Science4CleanEnergy (S4CE) research consortium, which was funded by European Union's Horizon 2020 research and innovation programme, under grant agreement ID: 764810.

References

(1) IEA. *World Energy Outlook 2020*; 2020. DOI: 10.1787/20725302.

(2) IEA. *Global Energy Review 2021*; 2021. DOI: 10.1787/a60abbf2-en.

(3) Kuuskraa, V. A.; Stevens, S. H.; Moodhe, K. Shale Gas Resources: An Assessment of 137 Shale Formations in 41 Countries Outside the United States. *Washingt. Indep. Stat. Anal. US Dep. Energy* **2013**, No. June.

(4) Ilgen, A. G.; Heath, J. E.; Akkutlu, I. Y.; Bryndzia, L. T.; Cole, D. R.; Kharaka, Y. K.; Kneafsey, T. J.; Milliken, K. L.; Pyrak-Nolte, L. J.; Suarez-Rivera, R. Shales at All Scales: Exploring Coupled Processes in Mudrocks. *Earth-Science Rev.* **2017**, *166*, 132–152. DOI: 10.1016/j.earscirev.2016.12.013.

(5) Josh, M.; Esteban, L.; Delle Piane, C.; Sarout, J.; Dewhurst, D. N.; Clennell, M. B. Laboratory Characterisation of Shale Properties. *J. Pet. Sci. Eng.* **2012**, *88–89*, 107–124. DOI: 10.1016/j.petrol.2012.01.023.

(6) Saraji, S.; Piri, M. The Representative Sample Size in Shale Oil Rocks and Nano-Scale Characterization of Transport Properties. *Int. J. Coal Geol.* **2015**, *146*, 42–54. DOI: 10.1016/j.coal.2015.04.005.

(7) Striolo, A.; Cole, D. R. Understanding Shale Gas: Recent Progress and Remaining Challenges. *Energy and Fuels* **2017**, *31* (10), 10300–10310. DOI: 10.1021/acs.energyfuels.7b01023.

(8) Wang, J.; Dong, M.; Yang, Z.; Gong, H.; Li, Y. Investigation of Methane Desorption and Its Effect on the Gas Production Process from Shale: Experimental and Mathematical Study. *Energy & Fuels* **2017**, *31* (1), 205–216. DOI: 10.1021/acs.energyfuels.6b02033.

(9) Ishida, T.; Aoyagi, K.; Niwa, T.; Chen, Y.; Murata, S.; Chen, Q.; Nakayama, Y. Acoustic Emission Monitoring of Hydraulic Fracturing Laboratory Experiment with Supercritical and Liquid CO2. *Geophys. Res. Lett.* **2012**, *39* (16). DOI: 10.1029/2012GL052788.

(10) Fathi, E.; Akkutlu, I. Y. Multi-Component Gas Transport and Adsorption Effects during CO2 Injection and Enhanced Shale Gas Recovery. *Int. J. Coal Geol.* **2014**, *123*, 52–61. DOI: 10.1016/j.coal.2013.07.021.

(11) Hughes, J. D. Energy: A Reality Check on the Shale Revolution. *Nature* **2013**, *494* (7437), 307–308. DOI: 10.1038/494307a.

(12) King, G. E. Thirty Years of Gas Shale Fracturing: What Have We Learned? *Proceedings - SPE Annual Technical Conference and Exhibition*. September 19, 2010, pp 900–949. DOI: 10.2118/133456-ms.

(13) Baihly, J.; Altman, R.; Malpani, R.; Luo, F. Shale Gas Production Decline Trend Comparison over Time and Basins. *Proceedings - SPE Annual Technical Conference and Exhibition*. September 19, 2010, pp 5276–5300. DOI: 10.2118/135555-ms.

(14) Krevelen, D. W. van. *Coal : Typology, Physics, Chemistry, Constitution*, 3rd ed.; Elsevier: Amsterdam , 1993.

(15) Horsfield, B.; Rullkötter, J. Diagenesis,Catagenesis, and Metagenesis of Organic Matter. *The Petroleum System—From Source to Trap*. American Association of Petroleum Geologists January 1, 1994, p 0. DOI: 10.1306/M60585C10.

(16) Selley, R. C. Sedimentary Rocks: Mineralogy and Classification. In *Encyclopedia of Geology*; Selley, R. C., Cocks, L. R. M., Plimer, I. R. B. T.-E. of G., Eds.; Elsevier: Oxford, 2004; pp 25–37. DOI: 10.1016/B0-12-369396-9/00304-X.

(17) Zhou, S.; Xue, H.; Ning, Y.; Guo, W.; Zhang, Q. Experimental Study of Supercritical Methane Adsorption in Longmaxi Shale: Insights into the Density of Adsorbed Methane. *Fuel* **2018**, *211*, 140–148. DOI: 10.1016/j.fuel.2017.09.065.

(18) Charoensuppanimit, P.; Mohammad, S. A.; Gasem, K. A. M. Measurements and Modeling of Gas Adsorption on Shales. *Energy and Fuels* **2016**, *30* (3), 2309–2319. DOI: 10.1021/acs.energyfuels.5b02751.

(19) Li, J.; Zhou, S.; Gaus, G.; Li, Y.; Ma, Y.; Chen, K.; Zhang, Y. Characterization of Methane Adsorption on Shale and Isolated Kerogen from the Sichuan Basin under Pressure up to 60 MPa: Experimental Results and Geological Implications. *Int. J. Coal Geol.* **2018**, *189*, 83–93. DOI: 10.1016/j.coal.2018.02.020.

(20) Zhao, H.; Lai, Z.; Firoozabadi, A. Sorption Hysteresis of Light Hydrocarbons and Carbon Dioxide in Shale and Kerogen. *Sci. Rep.* **2017**, *7* (1), 16209. DOI: 10.1038/s41598-017-13123-7.

(21) Wu, T.; Zhao, H.; Tesson, S.; Firoozabadi, A. Absolute Adsorption of Light Hydrocarbons and Carbon Dioxide in Shale Rock and Isolated Kerogen. *Fuel* **2019**, *235*, 855–867. DOI: 10.1016/j.fuel.2018.08.023.

(22) Zhao, H.; Wu, T.; Firoozabadi, A. High Pressure Sorption of Various Hydrocarbons and Carbon Dioxide in Kimmeridge Blackstone and Isolated Kerogen. *Fuel* **2018**, *224*, 412–423. DOI: 10.1016/j.fuel.2018.02.186.

(23) Sanguinito, S.; Goodman, A.; Tkach, M.; Kutchko, B.; Culp, J.; Natesakhawat, S.; Fazio, J.; Fukai, I.; Crandall, D. Quantifying Dry Supercritical CO2-Induced Changes of the Utica Shale. *Fuel* **2018**, *226*, 54–64. DOI: 10.1016/j.fuel.2018.03.156.

(24) Kelemen, S. R.; Afeworki, M.; Gorbaty, M. L.; Sansone, M.; Kwiatek, P. J.; Walters, C. C.; Freund, H.; Siskin, M.; Bence, A. E.; Curry, D. J.; Solum, M.; Pugmire, R. J.; Vandenbroucke, M.; Leblond, M.; Behar, F. Direct Characterization of Kerogen by X-Ray and Solid-State 13C Nuclear Magnetic Resonance Methods. *Energy and Fuels* **2007**, *21* (3), 1548–1561. DOI: 10.1021/ef060321h.

(25) Behar, F.; Vandenbroucke, M. Chemical Modelling of Kerogens. *Org. Geochem.* **1987**, *11* (1), 15–24. DOI: 10.1016/0146-6380(87)90047-7.

(26) Zhang, L.; LeBoeuf, E. J. A Molecular Dynamics Study of Natural Organic Matter: 1. Lignin, Kerogen and Soot. *Org. Geochem.* **2009**, *40* (11), 1132–1142. DOI: 10.1016/j.orggeochem.2009.08.002.

(27) Siskin, M.; Scouten, C. G.; Rose, K. D.; Aczel, T.; Colgrove, S. G.; Pabst, R. E. Detailed Structural Characterization of the Organic Material in Rundle Ramsay Crossing and Green River Oil Shales. In *Composition, Geochemistry and Conversion of Oil Shales*; Snape, C., Ed.; Springer Netherlands: Dordrecht, 1995; pp 143–158. DOI: 10.1007/978-94-011-0317-6_9.

(28) Orendt, A. M.; Pimienta, I. S. O.; Badu, S. R.; Solum, M. S.; Pugmire, R. J.; Facelli, J. C.; Locke, D. R.; Chapman, K. W.; Chupas, P. J.; Winans, R. E. Three-Dimensional Structure of the Siskin Green River Oil Shale Kerogen Model: A Comparison between Calculated and Observed Properties. *Energy and Fuels* **2013**, *27* (2), 702–710. DOI: 10.1021/ef3017046.

(29) Zhang, Z.; Jamili, A. Modeling the Kerogen 3D Molecular Structure. *Soc. Pet. Eng. - SPE/CSUR Unconv. Resour. Conf.* **2015**, 1–14. DOI: 10.2118/175991-ms.

(30) Ungerer, P.; Collell, J.; Yiannourakou, M. Molecular Modeling of the Volumetric and Thermodynamic Properties of Kerogen: Influence of Organic Type and Maturity. *Energy and Fuels* **2015**, *29* (1), 91–105. DOI: 10.1021/ef502154k.

(31) Lee, H.; Shakib, F. A.; Liu, K.; Liu, B.; Bubach, B.; Varma, R. S.; Jang, H. W.; Shokouhimher, M.; Ostadhassan, M. Adsorption Based Realistic Molecular Model of Amorphous Kerogen. *RSC Adv.* **2020**, *10* (39), 23312–23320. DOI: 10.1039/d0ra04453a.

(32) Ho, T. A.; Criscenti, L. J.; Wang, Y. Nanostructural Control of Methane Release in Kerogen and Its Implications to Wellbore Production Decline. *Sci. Rep.* **2016**, *6* (June), 1–9. DOI: 10.1038/srep28053.

(33) Ho, T. A.; Wang, Y.; Xiong, Y.; Criscenti, L. J. Differential Retention and Release of CO2 and CH4 in Kerogen Nanopores: Implications for Gas Extraction and Carbon Sequestration. *Fuel* **2018**, *220* (January), 1–7. DOI: 10.1016/j.fuel.2018.01.106.

(34) Ho, T. A.; Wang, Y.; Criscenti, L. J. Chemo-Mechanical Coupling in Kerogen Gas Adsorption/Desorption. *Phys. Chem. Chem. Phys.* **2018**, *20* (18), 12390–12395. DOI: 10.1039/c8cp01068d.

(35) Kazemi, M.; Maleki, H.; Takbiri-Borujeni, A. Molecular Dynamics Study of Transport and Storage of Methane in Kerogen. *SPE East. Reg. Meet.* **2016**, *2016-Janua* (September), 13–15. DOI: 10.2118/184058-MS.

(36) Michalec, L.; Lísal, M. Molecular Simulation of Shale Gas Adsorption onto Overmature Type II Model Kerogen with Control Microporosity. *Mol. Phys.* **2017**, *115* (9–12), 1086–1103. DOI: 10.1080/00268976.2016.1243739.

(37) Sui, H.; Yao, J. Effect of Surface Chemistry for CH4/CO2 Adsorption in Kerogen: A Molecular Simulation Study. *J. Nat. Gas Sci. Eng.* **2016**, *31*, 738–746. DOI: 10.1016/j.jngse.2016.03.097.

(38) Wang, Z.; Li, Y.; Liu, H.; Zeng, F.; Guo, P.; Jiang, W. Study on the Adsorption, Diffusion and Permeation Selectivity of Shale Gas in Organics. *Energies* **2017**, *10* (1), 1–15. DOI: 10.3390/en10010142.

(39) Pathak, M.; Kweon, H.; Deo, M.; Huang, H. Kerogen Swelling and Confinement: Its Implication on Fluid Thermodynamic Properties in Shales. *Sci. Rep.* **2017**, *7* (1), 12530. DOI: 10.1038/s41598-017-12982-4.

(40) Vasileiadis, M.; Peristeras, L. D.; Papavasileiou, K. D.; Economou, I. G. Modeling of Bulk Kerogen Porosity: Methods for Control and Characterization. *Energy and Fuels* **2017**, *31* (6), 6004–6018. DOI: 10.1021/acs.energyfuels.7b00626.

(41) Martin, M. G.; Siepmann, J. I. Transferable Potentials for Phase Equilibria. 1. United-Atom Description of n -Alkanes. *J. Phys. Chem. B* **1998**, *102* (14), 2569–2577. DOI: 10.1021/jp972543+.

(42) Vasileiadis, M.; Peristeras, L. D.; Papavasileiou, K. D.; Economou, I. G. Transport Properties of Shale Gas in Relation to Kerogen Porosity. *J. Phys. Chem. C* **2018**, *122* (11), 6166–6177. DOI: 10.1021/acs.jpcc.8b00162.

(43) Zhao, T.; Li, X.; Zhao, H.; Li, M. Molecular Simulation of Adsorption and Thermodynamic Properties on Type II Kerogen: Influence of Maturity and Moisture Content. *Fuel* **2017**, *190*, 198–207. DOI: 10.1016/j.fuel.2016.11.027.

(44) Huang, L.; Ning, Z.; Wang, Q.; Qi, R.; Cheng, Z.; Wu, X.; Zhang, W.; Qin, H. Molecular Insights into Kerogen Deformation Induced by CO2/CH4 Sorption: Effect of Maturity and Moisture. *Energy and Fuels* **2019**, *33* (6), 4792–4805. DOI: 10.1021/acs.energyfuels.9b00409.

(45) Alafnan, S.; Solling, T.; Mahmoud, M. Effect of Kerogen Thermal Maturity on Methane Adsorption Capacity: A Molecular Modeling Approach. *Molecules* **2020**, *25* (16). DOI: 10.3390/molecules25163764.

(46) Tesson, S.; Firoozabadi, A. Methane Adsorption and

Self-Diffusion in Shale Kerogen and Slit Nanopores by Molecular Simulations. *J. Phys. Chem. C* **2018**, *122* (41), 23528–23542. DOI: 10.1021/acs.jpcc.8b07123.

(47) Wu, T.; Firoozabadi, A. Effect of Microstructural Flexibility on Methane Flow in Kerogen Matrix by Molecular Dynamics Simulations. *J. Phys. Chem. C* **2019**, *123* (17), 10874–10880. DOI: 10.1021/acs.jpcc.8b12328.

(48) He, J.; Ju, Y.; Lammers, L.; Kulasinski, K.; Zheng, L. Tortuosity of Kerogen Pore Structure to Gas Diffusion at Molecular- and Nano-Scales: A Molecular Dynamics Simulation. *Chem. Eng. Sci.* **2020**, *215*, 115460. DOI: 10.1016/j.ces.2019.115460.

(49) Rezlerová, E.; Brennan, J. K.; Lísal, M. Methane and Carbon Dioxide in Dual-Porosity Organic Matter: Molecular Simulations of Adsorption and Diffusion. *AIChE J.* **2020**, No. April 2020, 1–17. DOI: 10.1002/aic.16655.

(50) Sun, Q.; Liu, W.; Zhang, N. Molecular Insights into Recovery of Shale Gas by CO2 Injection in Kerogen Slit Nanopores. *J. Nat. Gas Sci. Eng.* **2021**, *90* (February), 103903. DOI: 10.1016/j.jngse.2021.103903.

(51) Li, W.; Zhang, M.; Nan, Y.; Pang, W.; Jin, Z. Molecular Dynamics Study on CO2 Storage in Water-Filled Kerogen Nanopores in Shale Reservoirs: Effects of Kerogen Maturity and Pore Size. *Langmuir* **2021**. DOI: 10.1021/acs.langmuir.0c03232.

(52) Chong, L.; Sanguinito, S.; Goodman, A. L.; Myshakin, E. M. Molecular Characterization of Carbon Dioxide, Methane, and Water Adsorption in Micropore Space of Kerogen Matrix. *Fuel* **2021**, *283*, 119254.

(53) Huang, L.; Ning, Z.; Wang, Q.; Qi, R.; Zeng, Y.; Qin, H.; Ye, H.; Zhang, W. Molecular Simulation of Adsorption Behaviors of Methane, Carbon Dioxide and Their Mixtures on Kerogen: Effect of Kerogen Maturity and Moisture Content. *Fuel* **2018**, *211* (September 2017), 159–172. DOI: 10.1016/j.fuel.2017.09.060.

(54) Zhou, W.; Zhang, Z.; Wang, H.; Yang, X. Molecular Investigation of CO2/CH4 Competitive Adsorption and Confinement in Realistic Shale Kerogen. *Nanomaterials* **2019**, *9* (12). DOI: 10.3390/nano9121646.

(55) Li, Z.; Yao, J.; Firoozabadi, A. Kerogen Swelling in Light Hydrocarbon Gases and Liquids and Validity of Schroeder's Paradox. *J. Phys. Chem. C* **2021**, *125* (15), 8137–8147. DOI: 10.1021/acs.jpcc.0c10362.

(56) Schroeder, P. von. Über Erstarrungs- Und Quellugserscheinungen von Gelatine. *Zeitschrift für Phys. Chemie* **1903**, *45U* (1), 75–117. DOI: 10.1515/zpch-1903-4503.

(57) Clarkson, C. R.; Solano, N.; Bustin, R. M.; Bustin, A. M. M.; Chalmers, G. R. L.; He, L.; Melnichenko, Y. B.; Radliński, A. P.; Blach, T. P. Pore Structure Characterization of North American Shale Gas Reservoirs Using USANS/SANS, Gas Adsorption, and Mercury Intrusion. *Fuel* **2013**, *103*, 606–616. DOI: 10.1016/j.fuel.2012.06.119.

(58) Berthonneau, J.; Obliger, A.; Valdenaire, P. L.; Grauby, O.; Ferry, D.; Chaudanson, D.; Levitz, P.; Kim, J. J.; Ulm, F. J.; Pellenq, R. J. M. Mesoscale Structure, Mechanics, and Transport Properties of Source Rocks' Organic Pore Networks. *Proc. Natl. Acad. Sci. U. S. A.* **2018**, *115* (49), 12365–12370. DOI: 10.1073/pnas.1808402115.

(59) Sun, H. Compass: An Ab Initio Force-Field Optimized for Condensed-Phase Applications - Overview with Details on Alkane and Benzene Compounds. *J. Phys. Chem. B* **1998**, *102* (38), 7338–7364. DOI: 10.1021/jp980939v.

(60) Hagler, A. T.; Lifson, S.; Dauber, P. Consistent Force Field Studies of Intermolecular Forces in Hydrogen-Bonded Crystals. 2. A Benchmark for the Objective Comparison of Alternative Force Fields. *J. Am. Chem. Soc.* **1979**, *101* (18), 5122–5130. DOI: 10.1021/ja00512a002.

(61) Mayo, S. L.; Olafson, B. D.; Goddard, W. A. DREIDING: A Generic Force Field for Molecular Simulations. *J. Phys. Chem.* **1990**, *94* (26), 8897–8909. DOI: 10.1021/j100389a010.

(62) Wang, J.; Wolf, R. M.; Caldwell, J. W.; Kollman, P. A.; Case, D. A. Development and Testing of a General Amber Force Field. *J. Comput. Chem.* **2004**, *25* (9), 1157–1174. DOI: 10.1002/jcc.20035.

(63) Harris, J. G.; Yung, K. H. Carbon Dioxide's Liquid-Vapor Coexistence Curve and Critical Properties as Predicted by a Simple Molecular Model. *J. Phys. Chem.* **1995**, *99* (31), 12021–12024. DOI: 10.1021/j100031a034.

(64) Berendsen, H. J. C.; Postma, J. P. M.; van Gunsteren, W. F.; Hermans, J. Interaction Models for Water in Relation to Protein Hydration; Pullman, B., Ed.; Springer Netherlands: Dordrecht, 1981; pp 331–342. DOI: 10.1007/978-94-015-7658-1_21.

(65) Dubbeldam, D.; Calero, S.; Ellis, D. E.; Snurr, R. Q. RASPA: Molecular Simulation Software for Adsorption and Diffusion in Flexible Nanoporous Materials. *Mol. Simul.* **2016**, *42* (2), 81–101. DOI: 10.1080/08927022.2015.1010082.

(66) Dubbeldam, D.; Torres-Knoop, A.; Walton, K. S. On the Inner Workings of Monte Carlo Codes. *Mol. Simul.* **2013**, *39* (14–15), 1253–1292. DOI: 10.1080/08927022.2013.819102.

(67) Abraham, M. J.; Murtola, T.; Schulz, R.; Páll, S.; Smith, J. C.; Hess, B.; Lindah, E. Gromacs: High Performance Molecular Simulations through Multi-Level Parallelism from Laptops to Supercomputers. *SoftwareX* **2015**, *1–2*, 19–25. DOI: 10.1016/j.softx.2015.06.001.

(68) Bussi, G.; Donadio, D.; Parrinello, M. Canonical Sampling through Velocity Rescaling. *J. Chem. Phys.* **2007**, *126* (1), 14101. DOI: 10.1063/1.2408420.

(69) Nosé, S. A Molecular Dynamics Method for Simulations in the Canonical Ensemble. *Mol. Phys.* **1984**, *52* (2), 255–268. DOI: 10.1080/00268978400101201.

(70) Hoover, W. G. Canonical Dynamics: Equilibrium Phase-Space Distributions. *Phys. Rev. A* **1985**, *31* (3), 1695–1697. DOI: 10.1103/PhysRevA.31.1695.

(71) Parrinello, M.; Rahman, A. Polymorphic Transitions in Single Crystals: A New Molecular Dynamics Method. *J. Appl. Phys.* **1981**, *52* (12), 7182–7190. DOI: 10.1063/1.328693.

(72) Essmann, U.; Perera, L.; Berkowitz, M. L.; Darden, T.; Lee, H.; Pedersen, L. G. A Smooth Particle Mesh Ewald Method. *J. Chem. Phys.* **1995**, *103* (19), 8577–8593. DOI: 10.1063/1.470117.

(73) Sarkisov, L.; Bueno-Perez, R.; Sutharson, M.; Fairen-Jimenez, D. Materials Informatics with PoreBlazer v4.0 and the CSD MOF Database. *Chem. Mater.* **2020**, *32* (23), 9849–9867. DOI: 10.1021/acs.chemmater.0c03575.

(74) Talu, O.; Myers, A. L. Reference Potentials for Adsorption of Helium, Argon, Methane, and Krypton in High-Silica Zeolites. *Colloids Surfaces A Physicochem. Eng. Asp.* **2001**, *187–188*, 83–93. DOI: 10.1016/S0927-7757(01)00628-8.

(75) Hirschfelder, J. O.; Curtiss, C. F.; Bird, R. B. *Molecular Theory of Gases and Liquids*; Curtiss, C. F. (Charles F., Bird, R. B. (Robert B., Laboratory, U. of W. N. R., Eds.; John Wiley & Sons: New York, 1954.

(76) Düren, T.; Millange, F.; Férey, G.; Walton, K. S.; Snurr, R. Q. Calculating Geometric Surface Areas as a Characterization Tool for Metal - Organic Frameworks. *J. Phys. Chem. C* **2007**, *111* (42), 15350–15356. DOI: 10.1021/jp074723h.

(77) Stankiewicz, A.; Ionkina, N.; Motherwell, B.; Bennett, B.; Wint, O.; Mastalerz, M. Kerogen Density Revisited - Lessons from the Duvernay Shale. *Soc. Pet. Eng. - Unconv. Resour. Technol. Conf. URTeC 2015* **2015**, 864–874. DOI: 10.2118/178647-ms.

(78) Facelli, J.; Pugmire, R.; Pimienta, I. *Atomistic Modeling of Oil Shale Kerogens and Asphaltenes along with Their Interactions with the Inorganic Mineral Matrix*; Pittsburgh, PA, and Morgantown, WV (United States), 2011. DOI: 10.2172/1113672.

(79) Okiongbo, K. S.; Aplin, A. C.; Larter, S. R. Changes in Type II Kerogen Density as a Function of Maturity: Evidence from the Kimmeridge Clay Formation. *Energy and Fuels* **2005**, *19* (6), 2495–2499. DOI: 10.1021/ef050194+.

(80) Jiménez, A.; Iglesias, M. J.; Laggoun-Défarge, F.; Suárez-Ruiz, I. Study of Physical and Chemical Properties of Vitrinites. Inferences on Depositional and Coalification Controls. *Chem. Geol.* **1998**, *150* (3–4), 197–221. DOI: 10.1016/S0009-2541(98)00048-5.

(81) Yiannourakou, M.; Ungerer, P.; Leblanc, B.; Rozanska, X.; Saxe, P.; Vidal-Gilbert, S.; Gouth, F.; Montel, F. Modé Lisation Moléculaire de l'adsorption Dans Les Solides Microporeux. *Oil Gas Sci. Technol.* **2013**, *68* (6), 977–994. DOI: 10.2516/ogst/2013134.

(82) Chalmers, G. R. L.; Marc Bustin, R. On the Effects of Petrographic Composition on Coalbed Methane Sorption. *Int. J. Coal Geol.* **2007**, *69* (4), 288–304. DOI: 10.1016/j.coal.2006.06.002.

(83) Lu, X. C.; Li, F. C.; Watson, A. T. Adsorption Measurements in Devonian Shales. *Fuel* **1995**, *74* (4), 599–603. DOI: 10.1016/0016-2361(95)98364-K.

(84) Chalmers, G. R. L.; Bustin, R. M. The Organic Matter Distribution and Methane Capacity of the Lower Cretaceous Strata of Northeastern British Columbia, Canada. *Int. J. Coal Geol.* **2007**, *70* (1-3 SPEC. ISS.), 223–239. DOI: 10.1016/j.coal.2006.05.001.

(85) Rexer, T. F.; Mathia, E. J.; Aplin, A. C.; Thomas, K. M. High-Pressure Methane Adsorption and Characterization of Pores in Posidonia Shales and Isolated Kerogens. *Energy and Fuels* **2014**, *28* (5), 2886–2901. DOI: 10.1021/ef402466m.

(86) Zhang, T.; Ellis, G. S.; Ruppel, S. C.; Milliken, K.; Yang, R. Effect of Organic-Matter Type and Thermal Maturity on Methane Adsorption in Shale-Gas Systems. *Org. Geochem.* **2012**, *47*, 120–131. DOI: 10.1016/j.orggeochem.2012.03.012.

(87) Loucks, R. G.; Reed, R. M.; Ruppel, S. C.; Hammes, U. Spectrum of Pore Types and Networks in Mudrocks and a Descriptive Classification for Matrix-Related Mudrock Pores. *Am. Assoc. Pet. Geol. Bull.* **2012**, *96* (6), 1071–1098. DOI: 10.1306/08171111061.

(88) Eberle, A. P. R.; King, H. E.; Ravikovitch, P. I.; Walters, C. C.; Rother, G.; Wesolowski, D. J. Direct Measure of the Dense Methane Phase in Gas Shale Organic Porosity by Neutron Scattering. *Energy and Fuels* **2016**, *30* (11), 9022–9027. DOI: 10.1021/acs.energyfuels.6b01548.

(89) Bowers, G. M.; Loring, J. S.; Schaef, H. T.; Walter, E. D.; Burton, S. D.; Hoyt, D. W.; Cunniff, S. S.; Loganathan, N.; Kirkpatrick, R. J. Interaction of Hydrocarbons with Clays under Reservoir Conditions: In Situ Infrared and Nuclear Magnetic Resonance Spectroscopy and X-Ray Diffraction for Expandable Clays with Variably Wet Supercritical Methane. *ACS Earth Sp. Chem.* **2018**, *2* (7), 640–652. DOI: 10.1021/acsearthspacechem.8b00039.

(90) Bowker, K. A. Barnett Shale Gas Production, Fort Worth Basin: Issues and Discussion. *Am. Assoc. Pet. Geol. Bull.* **2007**, *91* (4), 523–533. DOI: 10.1306/06190606018.

(91) Sun, Y.; Li, S.; Sun, R.; Liu, X.; Pu, H.; Zhao, J. Study of CO2enhancing Shale Gas Recovery Based on Competitive Adsorption Theory. *ACS Omega* **2020**, *5* (36), 23429–23436. DOI: 10.1021/acsomega.0c03383.

Insert Table of Contents artwork here